Check for updates

Ultra-high efficiency bremsstrahlung production in the interaction of direct laser-accelerated electrons with high-Z material

P. Tavana[1,2]*, N. Bukharskii[3], M. Gyrdymov[2], U. Spillmann[4], Ş. Zähter[4,5], J. Cikhardt[6], N. G. Borisenko[3], Ph. Korneev[3], J. Jacoby[2], C. Spielmann[1], N. E. Andreev[7], M. M. Günther[4] and O. N. Rosmej[2,4]

[1]Institute of Optics and Quantum Electronics (IOQ), Friedrich Schiller University Jena, Jena, Germany, [2]Institute for Applied Physics (IAP), Goethe University Frankfurt, Frankfurt am Main, Germany, [3]P. N. Lebedev Physical Institute (LPI), Russian Academy of Sciences, Moscow, Russia, [4]GSI Helmholtzzentrum für Schwerionenforschung, Darmstadt, Germany, [5]Focused Energy GmbH, Darmstadt, Germany, [6]Faculty of Electrical Engineering, Czech Technical University in Prague, Prague, Czechia, [7]Joint Institute for High Temperatures, Russian Academy of Sciences, Moscow, Russia

High performance of laser-driven sources of radiation is in focus of research aimed at the study of high energy density matter, pair production and neutron generation using kJ PW-laser systems. In this work, we present a highly efficient approach to generate an ultra-high flux, high-energy bremsstrahlung in the interaction of direct laser-accelerated (DLA) electrons with a several-millimeters-thick high-Z converter. A directed beam of direct laser-accelerated electrons with energies up to 100 MeV was produced in the interaction of a sub-ps laser pulse of moderate relativistic intensity with long-scale plasma of near-critical density obtained by irradiation of low-density polymer foam with an ns laser pulse. In the experiment, tantalum isotopes generated via photonuclear reactions with threshold energies above 40 MeV were observed. The Geant4 Monte Carlo code, with the measured electron energy and angular distribution as input parameters, was used to characterize the bremsstrahlung spectrum responsible for the registered yields of isotopes from ^{180}Ta to ^{175}Ta. It is shown that when the direct laser-accelerated electrons interact with a tantalum converter, the directed bremsstrahlung with an average photon energy of 18 MeV and ~ 2 · 10^{11} photons per laser shot in the energy range of giant dipole resonance (GDR) and beyond (≥7.5 MeV) is produced. This results in an ultra-high photon flux of ~6 × 10^{22} sr^{-1}·s^{-1} and a record conversion efficiency of 2% of the focused laser energy into high-energy bremsstrahlung.
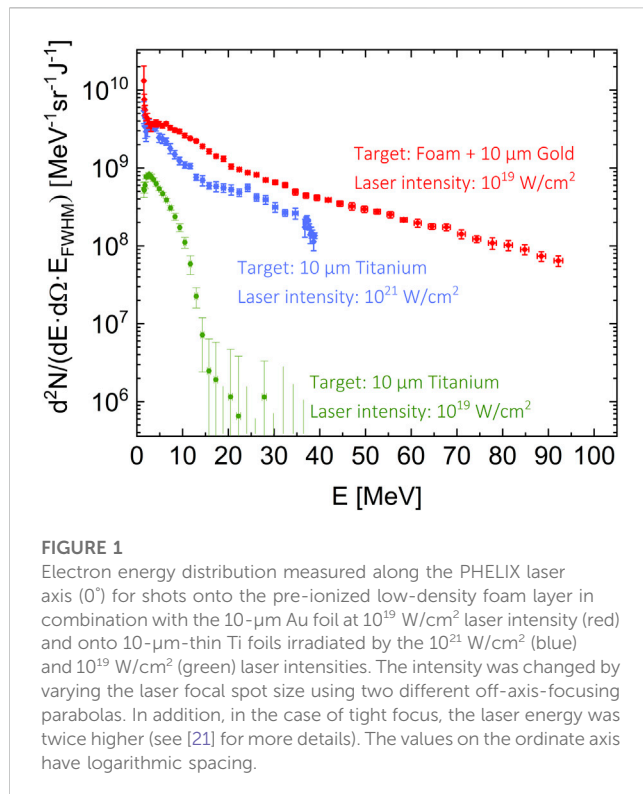
FIGURE 1
Electron energy distribution measured along the PHELIX laser axis (0°) for shots onto the pre-ionized low-density foam layer in combination with the 10-µm Au foil at 10^{19} W/cm^2 laser intensity (red) and onto 10-µm-thin Ti foils irradiated by the 10^{21} W/cm^2 (blue) and 10^{19} W/cm^2 (green) laser intensities. The intensity was changed by varying the laser focal spot size using two different off-axis-focusing parabolas. In addition, in the case of tight focus, the laser energy was twice higher (see [21] for more details). The values on the ordinate axis have logarithmic spacing.

1 Introduction

Intense x-ray and gamma-ray beams have potential novel applications in many research branches, including nuclear physics and laboratory astrophysics [1–3], proton activation analysis (PAA) in materials research [4–7], radiography of high-energy-density (HED) matter [7], electron–positron pair production [8], and medical isotope production for radiation oncology [9]. In addition, nuclear resonance fluorescence (NRF) studies are attractive for the development of isotope selective techniques [10]. One of the most robust mechanisms of high-energy photon generation is bremsstrahlung (BS) of electrons decelerated in the field of nuclei [11].

Short-pulse laser systems with intensity above 10^{18} W/cm^2 provide great possibilities for generation of pulsed sources of particles and radiation, where laser-accelerated electrons play a major role in coupling of the laser energy to matter. In the laser–plasma interaction, copious amounts of relativistic multi-MeV electrons can be produced, which are accelerated via physical processes that depend on the target design and the interaction conditions. These processes are Brunel effect [12, 13], pondermotive ($j \times B$) acceleration [14, 15], laser wakefield acceleration (LWFA) [16, 17], direct laser acceleration [18–21], stochastic heating [22], etc. When theses relativistic electrons propagate in a high atomic number thick solid target located behind the interaction area, MeV bremsstrahlung photons are produced. The energy spectrum and number of high-energy photons depend on the energy distribution, the total charge of accelerated electrons, and the target properties.

Experiments on laser-driven bremsstrahlung sources of x-rays and MeV gamma-rays produced in high-Z materials can usually be divided into two groups depending on the target setup, where in the first case, the laser interacts directly with a solid-state high-Z converter and in the second case, an electron beam is generated

in a plasma target and then penetrates into a "cold" converter. Different diagnostic methods can be used to detect and reconstruct BS spectrum, depending on the photon energy range. An important method is the activation technique [23–25], which provides access to the region of giant dipole resonance (GDR) with photon energies beyond 7.5 MeV. The nuclear activation technique was also successfully applied to investigate the hot electron distribution in the interaction of multi-petawatt laser pulses with a high-Z target, where by comparing different activation ratios of isotopes produced in photonuclear reactions, the temperature of hot electrons was determined [26–28].

Experiments using direct laser irradiation of the high-Z converter for production of MeV bremsstrahlung radiation were reported for high-energy lasers such as VULCAN [23] and NOVA [24] with $\sim10^{10}$ photons in the range of giant dipole resonance (GDR) and up to 0.2% laser-BS conversion efficiency measured by means of the nuclear activation technique. In an experiment on the Texas Petawatt Laser [29], the multi-millimeter thick gold target was directly irradiated with an ultra-relativistic laser pulse of $\geq10^{21}$ W/cm^2 intensity. A conversion efficiency of 2% was estimated for the photon spectrum with an average energy of 6 MeV in the energy range from 3 to 50 MeV, measured by forward Compton scattering.

To improve the BS production efficiency, the initial stage, namely, the acceleration of electrons, can be separated from the subsequent stage of converting electrons to BS. This can be realized in different ways, as demonstrated in the following works. Electron beams generated in the interaction of relativistic laser pulses with an under-dense plasma medium (e.g., gas jet) via LWFA can reach GeV energies and carry sub-nC charges. As reported in [30], on experiments with a DRACO laser ($\sim10^{19}$ W/cm^2), the interaction of such an electron beam with an 800-µm-thick Ta converter led to the generation of $\sim 4 \times 10^8$ photons with an average energy of 30–40 MeV and an estimated conversion efficiency of 0.1%. In this work, photon energy distribution was measured by the differential filter method and analyzed with Monte Carlo simulations.

One can increase the density of the plasma jet and switch to the self-modulated (SM) LWFA [31], which leads to a higher charge of generated MeV electrons and correspondingly higher conversion efficiency. SM LWFA is a platform for x-ray and gamma-ray production for probing the HED matter at NIF [32]. Production of high-energy high-current electron beams with charge up to 10 nC ($E_e > 1.2$ MeV) was demonstrated in the interaction of 10^{20} W/cm^2 laser pulse with high-density argon gas jet [33]. Millimeter-thick copper targets were used as converters. The measured BS spectrum with a cut-off energy of 15 MeV showed an exponential distribution with $T_1 = 0.49$ MeV for the low-energy part and $T_2 = 3.8$ MeV for the high-energy part and a total number of photons with energy ≤15 MeV of 10^{10} directed in 20.5° (FWHM).

By further increasing the density of plasma up to the critical electron density (e.g., 10^{21} cm^{-3} for 1 µm laser wavelength), one may enter the domain of the direct laser acceleration mechanism (DLA) predicted in [34–39] and demonstrated experimentally in [19–21, 40, 41]. In case of tens of fs short pulses, this mechanism was realized in experiments with double-layer targets [39, 41], where a foam layer of a few µm thickness was grown on top of the metal foil. When changing from fs to ps high-energy laser systems, the foam thickness must be greatly increased. In experiments with the PHELIX [42] high-power laser, sub-millimeter-long polymer aerogels [43] pre-ionized with the 10^{13} W/cm^2 ns laser
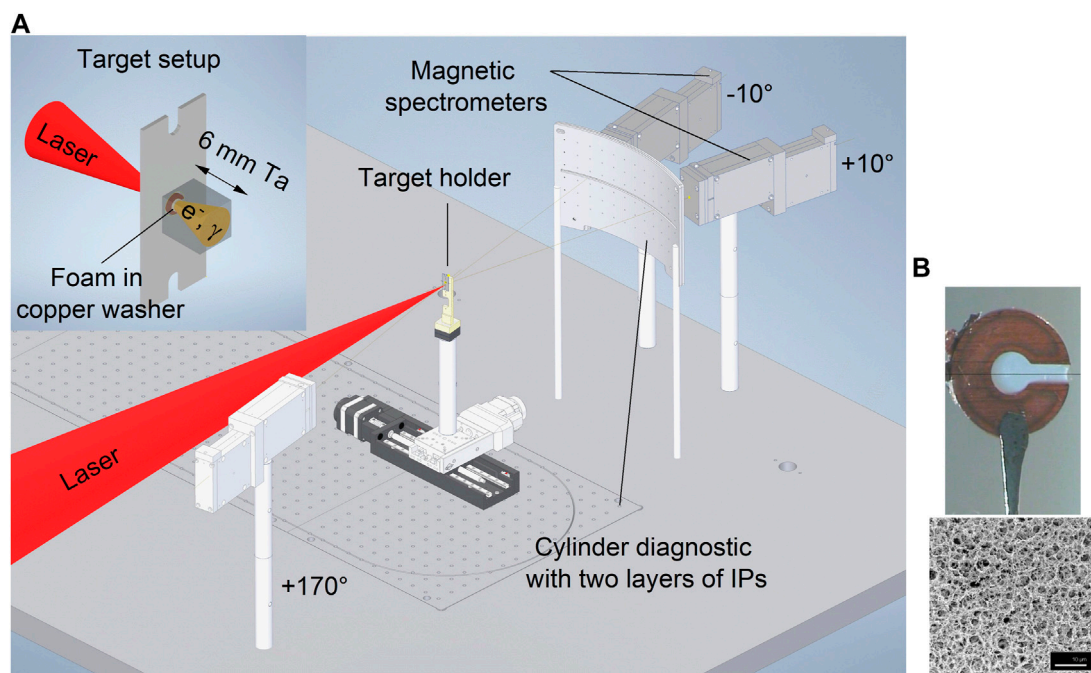
FIGURE 2
(A) Schematic view of the experimental and target (see inset) setup. **(B)** Foam target in the copper washer and SEM picture of the CHO foam structure.

TABLE 1 Nuclear reaction data for the photonuclear reaction in tantalum.

Reaction	Nuclide	Half-life	Energy/keV (intensity)	Threshold (MeV)	Peak (MeV)	Peak σ(mb)
^{181}Ta(γ, n)	^{180}Ta	8.152 h	93.32 (4.5%) and 103.55 (0.81%)	7.57	12.7	347
^{181}Ta(γ, $2n$)	^{179}Ta	1.82 y	-	14.22	16	203
^{181}Ta(γ, $3n$)	^{178}Ta	9.31 min	93.18 (6.6%) and 1,350.61 (1.18%)	22.05	28	10.6
^{181}Ta(γ, $3n$)	^{178m}Ta	2.36 h	426.38 (97%), 325.56 (94.1%), and 213.44 (81.4%)	22.35	27	9
^{181}Ta(γ, $4n$)	^{177}Ta	56.56 h	112.94 (7.2%)	29.01	38	10.5
^{181}Ta(γ, $5n$)	^{176}Ta	8.09 h	1,159.28 (25%), 1,224.93 (6%), and 710.50 (5%)	37.43	46	7.3
^{181}Ta(γ, $6n$)	^{175}Ta	10.5 h	207.4 (14%) and 348.5 (12%)	44.46	55.5	6.8

pulse that preceded the relativistic ps-pulse were used. The thickness of the 2 -mg/cm³ foam layers was in the range of 300–1000 μm in order to provide a long acceleration path for the DLA electrons. Experiments with laser pulses of ~10^{19} W/cm² intensity showed up to 40% conversion efficiency of the laser energy into electrons with an energy above the ponderomotive potential of 1.5 MeV and a higher number of relativistic electrons (> 30 MeV) in comparison with direct shots on metal foils at an ultra-relativistic laser intensity of 10^{21} W/cm², as shown in Figure 1 [21]. The effective temperature of the DLA electrons generated in such long-scale NCD plasma exceeds 10 times the pondermotive potential, and the charge of the accelerated electrons with energy above pondermotive potential reaches 1 μC.

In this paper, we show that the use of NCD plasma with a secondary high-Z target of several millimeters thickness allows for creation of the unprecedented high-energy and high-flux gamma source. The paper is

organized as follows: in Section 2, laser and target parameters, together with the used experimental set-up (Section 2.1) and the nuclear activation method (Section 2.2), are described. In Section 3, results on characterization of super-ponderomotive DLA electrons (Section 3.1), gamma spectroscopy measurements (Section 3.2), and the Geant4 simulations of bremsstrahlung and isotope production are presented. Section 4 summarizes the results.

2 Materials and methods

2.1 Experimental setup

The experiment was performed at the PHELIX (Petawatt High-Energy Laser for Heavy Ion EXperiments) laser facility at the
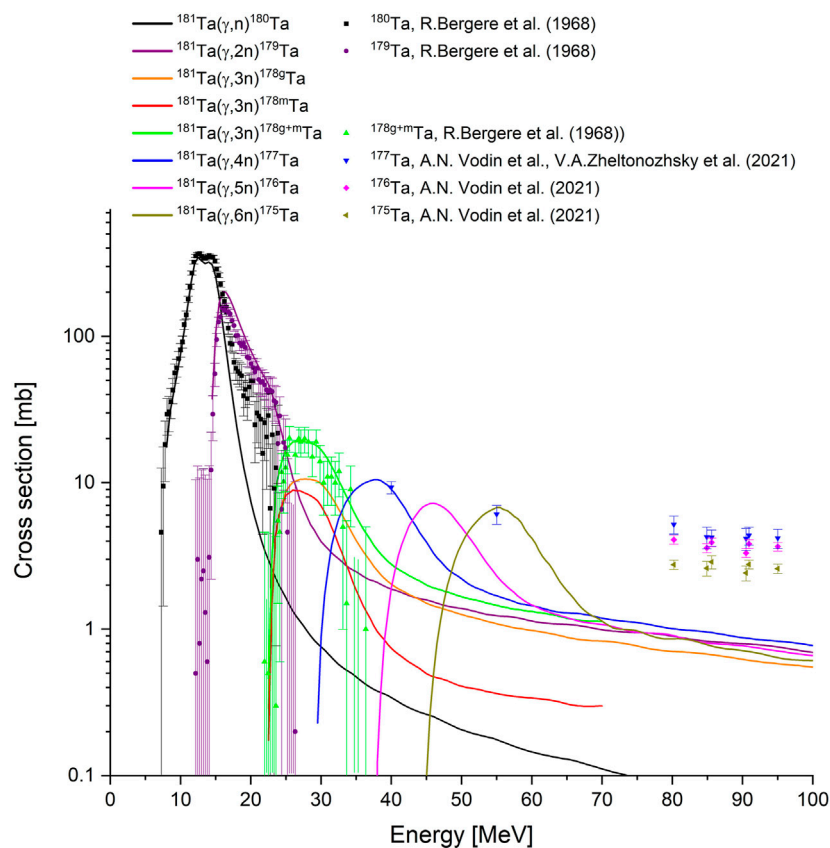
FIGURE 3
Cross sections for different ^{181}Ta (γ, xn) reactions simulated with TALYS code and from experimental data available from [46]. The values on the ordinate axis have logarithmic spacing.
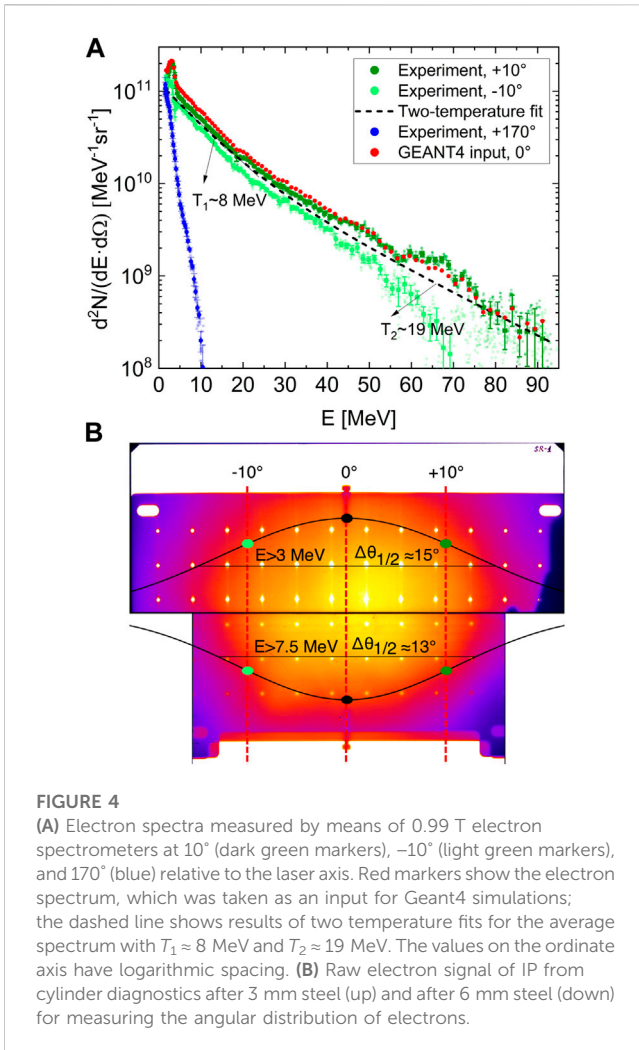
Helmholtzzentrum GSI, Darmstadt [42], in a single-shot mode. A ns pulse with an intensity of $\sim$10^{13} W/cm^2 and $\sim$70 mJ energy in the FWHM of the 15 μm × 12 μm focal spot was used to heat a foam target and to convert it into plasma of near critical density (NCD). A s-polarized, 750(250) fs PHELIX laser pulse of 75(5) J energy and wavelength of λ = 1.053 μm, focused by means of a 150-cm off-axis parabolic mirror, interacted with the pre-ionized 3-ns earlier foam target. Energy of 20(2) J is measured in FWHM of the focal spot, which corresponds to $\sim$25% of the total laser energy, so the intensity of the main pulse reaches $\sim$10^{19} W/cm^2 with a normalized laser vector potential amplitude a_0 = 2.9. The target normal was tilted 10° to the laser beam axis to avoid back reflection of the laser light. The foam target was made of CHO polymer aerogel of 2 mg/cm^3 density, 2.5 mm in diameter, and 1,000 μm thickness [20, 43]. Assuming the foam target is fully ionized by the ns pulse, this corresponds to 0.64×10^{21} cm^{-3} electron density or $0.64n_{cr}$ with $n_{cr} = 10^{21}$ cm^{-3} being the critical density for 1.053 μm laser wavelength. A tantalum converter of 4 mm × 4 mm in cross section and thickness of 6 mm was attached to the rear side of the foam target, which was grown inside a copper washer. This tantalum plate is used (1) to convert the hot electron kinetic energy into hard photons through the bremsstrahlung mechanism and (2) as a diagnostic tool to measure the number of Ta isotopes produced

due to (γ, xn) reactions. The experimental setup and the target design are shown in Figure 2.

For measuring the electron spectra in forward and backward directions, 0.99-T magnetic spectrometers were placed at ±10° and 170° to the laser axis. The distance of entrance slits of electron spectrometers to the interaction point is 455 mm for the electron spectrometers at ±10° and 375 mm for the 170° electron spectrometer. For measuring the angular distribution of electrons, two large area IPs were placed between three layers of 3-mm stainless steel semi-cylindrical plates with 300 mm curvature radius. The cylindrical stack (see Figure 2) was placed at 340 mm from the interaction point and covered 37° in the horizontal direction and 20° in the vertical direction. For more details about the electron spectrometers and the cylinder diagnostic, see [21].

2.2 Nuclear activation technique

A high-current directed beam of DLA electrons, produced in the interaction of the PHELIX laser pulse with NCD plasma, was sent to a Ta converter to generate BS radiation, which can be characterized in terms of yields of isotopes produced in photonuclear reactions [24, 25]. In this process, a high-energy

FIGURE 4
(A) Electron spectra measured by means of 0.99 T electron spectrometers at 10° (dark green markers), −10° (light green markers), and 170° (blue) relative to the laser axis. Red markers show the electron spectrum, which was taken as an input for Geant4 simulations; the dashed line shows results of two temperature fits for the average spectrum with $T_1 \approx 8$ MeV and $T_2 \approx 19$ MeV. The values on the ordinate axis have logarithmic spacing. **(B)** Raw electron signal of IP from cylinder diagnostics after 3 mm steel (up) and after 6 mm steel (down) for measuring the angular distribution of electrons.

photon excites the giant dipole resonances of nuclei and triggers photonuclear reactions. As a result, one or multiple neutrons are emitted. The formed compound nucleus is usually radioactive and emits characteristic gamma-quanta of certain energies. The decay spectra of the activated sample measured by means of gamma spectroscopy reveal the yield of the photonuclear reaction product, subject to the condition that the activity distribution of the sample is known. Then, the number of reactions (yield) Y is the convolution of the bremsstrahlung spectrum $\Phi(E_\gamma)$ and the energy-dependent cross section $\sigma(E_\gamma)$ of a photonuclear reaction [44]:

$$Y = N_T \int_{S_n}^{\infty} \sigma(E_\gamma)\Phi(E_\gamma)dE_\gamma, \qquad (1)$$

where S_n is the threshold energy of the reaction and N_T is the number of irradiated target atoms. By combining yields of different isotopes, it is possible to reconstruct the bremsstrahlung spectrum, as described in [3, 25, 28].

In this study, tantalum plates were used simultaneously as a converter and activation materials. They were composed of 99.9% ^{181}Ta, a stable tantalum isotope. Photo-nuclear activation in the tantalum target provides information on the
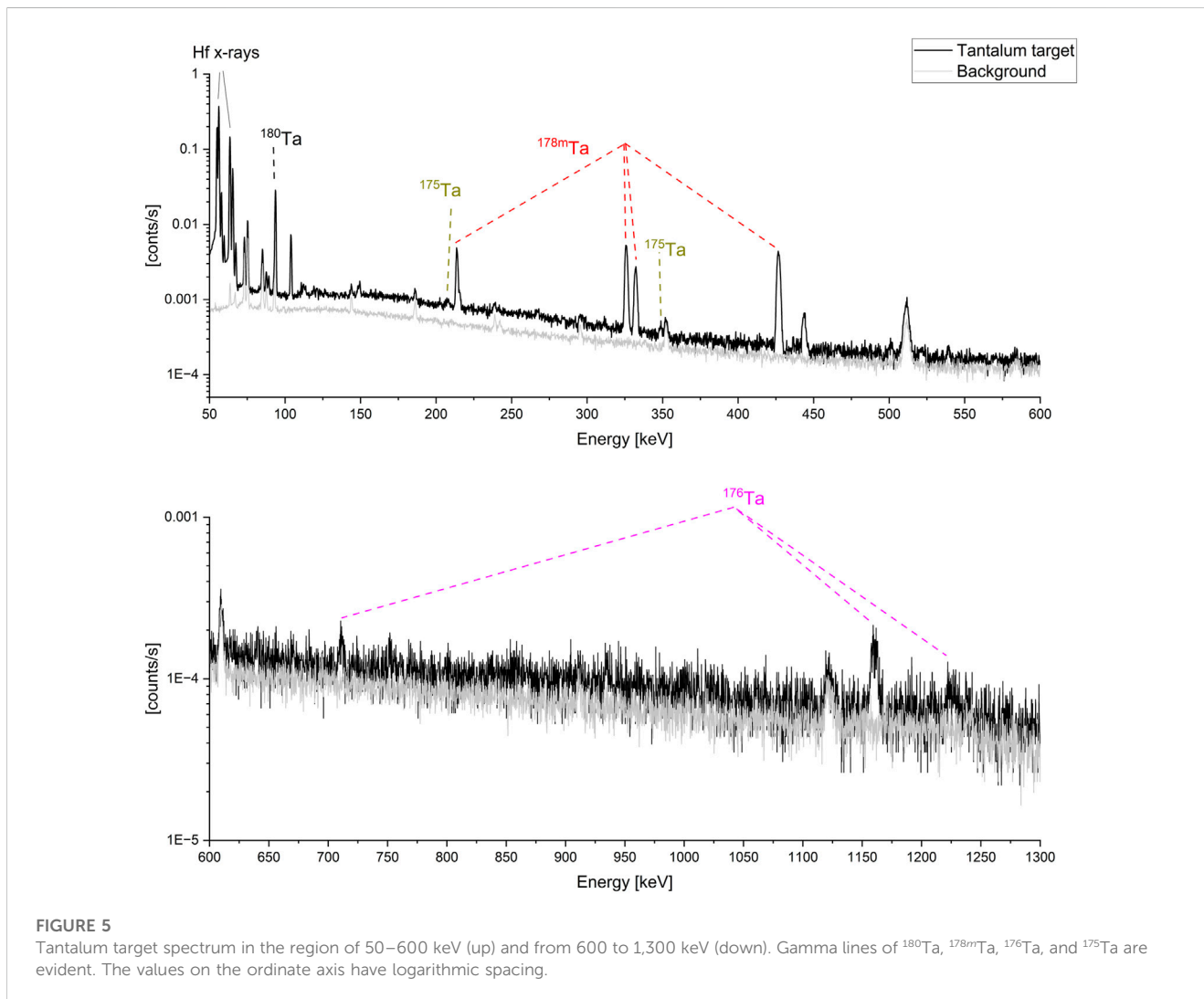
high-energy part of the bremsstrahlung spectrum with E > 7.5 MeV, which is fixed by the photonuclear cross section of the ^{181}Ta$(\gamma,n)^{180}$Ta reaction. The dependence of the cross-sections of different (γ, xn) reactions (where x is the number of neutrons, $1 \le x \le 6$) in ^{181}Ta on photon energy simulated with the nuclear reaction code TALYS [45], and the same dependence based on the experimental data from [46] are shown in Figure 3.

The isotope ^{180}Ta decays via electron capture (EC) (85%) with a half-life of 8.1 h to an excited state of ^{180}Hf, which then goes to the ground state by emission of a γ-quantum of 93 keV. Hf x-rays, $K_\alpha = 55.7$ keV, and $K_\beta = 63.2$ keV are also emitted in this process. The competing decay to EC is β^--decay, with the same characteristic half-life time of 8.1 h. This decay produces an excited state of ^{180}W, which achieves stability via emission of 103 keVγ-quantum. The product of the reaction ^{181}Ta$(\gamma,2n)$ ^{179}Ta has a half-life time of 664 d, which is too long for the type of analysis undertaken in this study. The reaction ^{181}Ta$(\gamma, 3n)$ can lead to the ground state of ^{178}Ta with a half-life time of 9.31 min, which decays via EC to the excited state of ^{178}Hf and emits γ-rays with energy 93.1 keV. Because the 93.13 keV γ-ray is also emitted by decay of ^{180}Ta, presence of the isotope ^{178}Ta is neglected. The reaction ^{181}Ta$(\gamma, 3n)$ can also lead to ^{178m}Ta, which decays via EC with a characteristic half-life time of 2.36 h to excited states of ^{178}Hf, which then achieves stability via the emission of a number of γ-quanta. Among them, the most intensive ones are 426.38, 325.562, and 213.44 keV. The product of ^{181}Ta$(\gamma, 5n)$ ^{176}Ta decays only via EC with a characteristic half-life time of 8.09 h to excited states of ^{176}Hf, the most prominent γ-quanta of 1,159 keV take 24.7%. The isotope ^{175}Ta also decays via EC to excited states of ^{175}Hf with a half-life time of 10.5 h and emits characteristic γ-quanta of different energies, including those with 207.4 and 348.5 keV. The threshold energies, the cross sections, the half-life times, and the characteristic energies of the reactions of the tantalum isotopes are summarized in Table 1.

3 Results and discussion

3.1 Experimental results on DLA electrons

Figure 4A shows the electron spectra registered by three 0.99-T magnetic spectrometers at ±10° and 170° to the laser axis with imaging plates (IPs) as detectors. The shot was made on the 800-μm-thick pre-ionized CHO foam target. The measured averaged spectrum for ±10° directions can be approximated by a Maxwellian-like distribution function with two temperatures: $d^2N/(dE \cdot d\Omega)[\text{MeV}^{-1}\text{sr}^{-1}] = 10^{11}$ $\exp\left(-\frac{E\,[\text{MeV}]}{8}\right) + 2.6 \cdot 10^{10} \exp\left(-\frac{E\,[\text{MeV}]}{19}\right)$. The maximum energy of electrons reaches 90 MeV at the level of $2e8\text{MeV}^{-1}\text{sr}^{-1}$. At the same time, ponderomotive electrons with an effective temperature of 1.2 MeV were observed in the backward direction at 170° to the laser axis. On the cylinder stack, we observe a collimated beam of electrons with energies E > 3 MeV (first IP) and E > 7.5 MeV (second IP) with divergence angles of 15° and 13°, respectively (Figure 4B). Using cylinder diagnostic and the electron spectrometers, the charge carried by electrons was estimated: the charge of electrons with E > 7.5 MeV, which propagate in the forward direction and are capable of generating
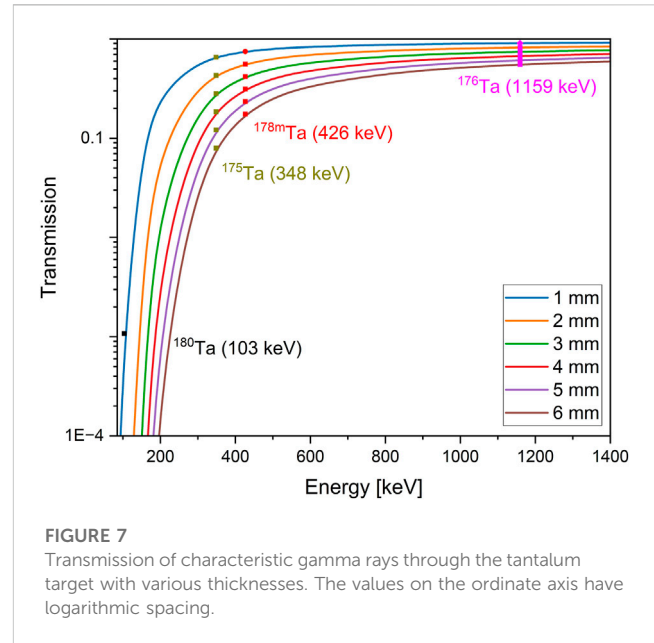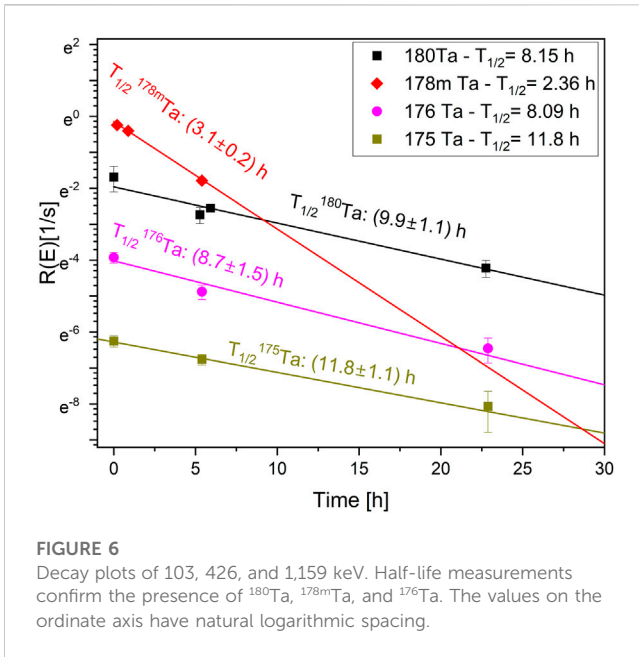
FIGURE 5
Tantalum target spectrum in the region of 50−600 keV (up) and from 600 to 1,300 keV (down). Gamma lines of ^{180}Ta, ^{178m}Ta, ^{176}Ta, and ^{175}Ta are evident. The values on the ordinate axis have logarithmic spacing.

gammas responsible for photonuclear reaction in tantalum, is of ~ 60 nC.

3.2 Experimental results on gamma spectroscopy

After the laser shot, the tantalum target was subjected to gamma spectral analysis using a coaxial p-type high-purity germanium detector (HPGe). The detector was shielded by lead bricks to reduce the contribution of background radiation in the laboratory. The signals from the detector were analyzed by a multichannel buffer (MCB) (Ortec MCB 928) using ORTEC Maestro software. For evaluating the gamma-ray spectra of the activated tantalum target, it is important to measure any contribution from background radiation. For this purpose, the spectrum of the background was taken over 7 days to improve the counting statistics, and then, the overall counting rate was normalized to the duration time of the tantalum target measurement. Figure 5 shows the gamma spectrum obtained from the tantalum converter in the region of 50–1,300 keV with

the background contribution after 63 h. To confirm independently the existence of isotopes ^{180}Ta, ^{178m}Ta, ^{176}Ta, and ^{175}Ta in addition to the characteristic γ-lines shown in Figure 5, the decay time of the states related to these γ-lines has been measured. The sample was measured for the total time of ~63 h, and various snapshots of the spectrum were saved for different time slots. In Figure 6, the number of γ-rays emitted per second, $R(E)$, for 103 keV(^{180}Ta), 426 keV (^{178m}Ta), 1,159 keV (^{176}Ta), and 346 keV (^{176}Ta) is shown as a function of time, where $t = 0$ is the start of measurement (82 min after the laser shot). The error bars come from uncertainty in fitting the full energy peak to the Gaussian distribution. A correction for the emission rates due to decay during the counting period has been determined. For 103 keV peak, the half-life time was found to be 9.9(11) h (accepted value is 8.15 h); for 426 keV, it was found to be 3.1(2) h (accepted value is 2.36 h); for 1,159 keV, it was 8.7(1.5) h (accepted value is 8.09 h); and for 348 keV, it was 11.8(1.1) h (accepted value is 10.5 h). Because the state of ^{177}Ta related to the 112.9 keV gamma-line has a low intensity and considerably large half-life time, the decay of this state could not be confirmed.

FIGURE 6
Decay plots of 103, 426, and 1,159 keV. Half-life measurements confirm the presence of ^{180}Ta, ^{178m}Ta, and ^{176}Ta. The values on the ordinate axis have natural logarithmic spacing.

FIGURE 7
Transmission of characteristic gamma rays through the tantalum target with various thicknesses. The values on the ordinate axis have logarithmic spacing.

Due to the narrow angular spread of the electron beam, the tantalum target is irradiated non-homogeneously, and it is not possible to determine the number of target atoms N_t needed to deduce the photon number from Eq. 1. Moreover, one has to take into account the absorption of gamma rays as they propagate through tantalum to HPGe detector's cap. In Figure 7, transmission of characteristic gamma rays for 1–6 mm thickness of tantalum is shown. To overcome these problems, Monte Carlo simulations were performed to calculate the yield of isotopes and to compare them with the experiment.

3.3 Monte Carlo simulations for bremsstrahlung production

To get a better insight into the electron beam interaction with the tantalum target, Monte Carlo simulations were performed to calculate bremsstrahlung generated by DLA electrons. For this, the Geant4 package was used, which takes into account both electromagnetic and hadronic processes [47, 48]. The input electron spectrum was taken from the experimental data presented in Figure 4A. The data are averaged using the data for ±10° shown in Figure 4A. For the electron angular distribution, a Gaussian-like profile was assumed in the form $k_{(10°\to0°)} \cdot \frac{f_{+10°}+f_{-10°}}{2} \exp\left(-\ln 2 \cdot \left(\frac{\theta}{\theta_{1/2}}\right)^2\right)$, where $f_{+10°}$ and $f_{-10°}$ are the experimentally measured electron number densities $d^2N/(dE \cdot d\Omega)$ at +10° and −10°, respectively, $\theta_{1/2} = 15°$, and the coefficient $k_{(10°\to0°)} = 1.36$ was introduced to retrieve the number of electrons at 0° direction based on the known angular profile of the electron beam measured by the cylinder diagnostic; see Figure 4B.

The resulting spectrum of electrons with energy > 1.5 MeV, which was then used as the input for Geant4, is shown with red markers in Figure 4A. As a converter, a tantalum box of 4 mm × 4 mm × 6 mm was used. The electron source was located at the center of the converter

front. Since the simulation for the real number of electrons was unfeasible due to high computational costs, in calculations, their number was reduced to a total of 10^8 particles, and this reduction was taken into account by appropriate normalization in the final results.

Due to the interaction of the relativistic electron beam with the material of the converter, MeV-scale bremsstrahlung was produced. The resultant fluences of both "low-energy" (<7.5 MeV) and "high-energy" (>7.5 MeV) primary and secondary electrons, and the produced BS radiation for the same energy ranges are shown in Figure 8.

For low-energy electrons, scattering in the target material plays a significant role, and the transverse size of the beam increases substantially in comparison with the value defined by the initial divergence of the electron beam. The high-energy electrons, in contrast, continue to propagate as a more collimated beam, penetrating a few millimeters inside tantalum before their energy drops below 7.5 MeV. The distribution of the gamma quanta for the low- and high-energy ranges generally follows the distribution of low- and high-energy electrons; however, their penetration depth for both <7.5 MeV and >7.5 MeV ranges is greater than that for electrons so that they can reach the opposite edge of the converter box. The obtained energy spectra of BS radiation in dependence of tantalum thickness for Z = 1 mm, Z = 3 mm, and Z = 6 mm presented in Figure 9 can be described by an exponential function with a mean photon energy of 5–6 MeV in the photon energy range 1.5–7.5 MeV and 18 MeV above 7.5 MeV. From the presented data, it can be seen that there is an optimal thickness of the converter at Z = 3 mm (green markers), where the fraction of high-energy photons is higher than that at Z = 1 mm and Z = 6 mm.

For the former, the target thickness is too low for the effective conversion of high-energy electrons into bremsstrahlung radiation, while for the latter, the fluence of photons starts to drop as a result of Compton scattering and gamma-induced pair production. At the same time, for Z > 3 mm, a significantly lower amount of new
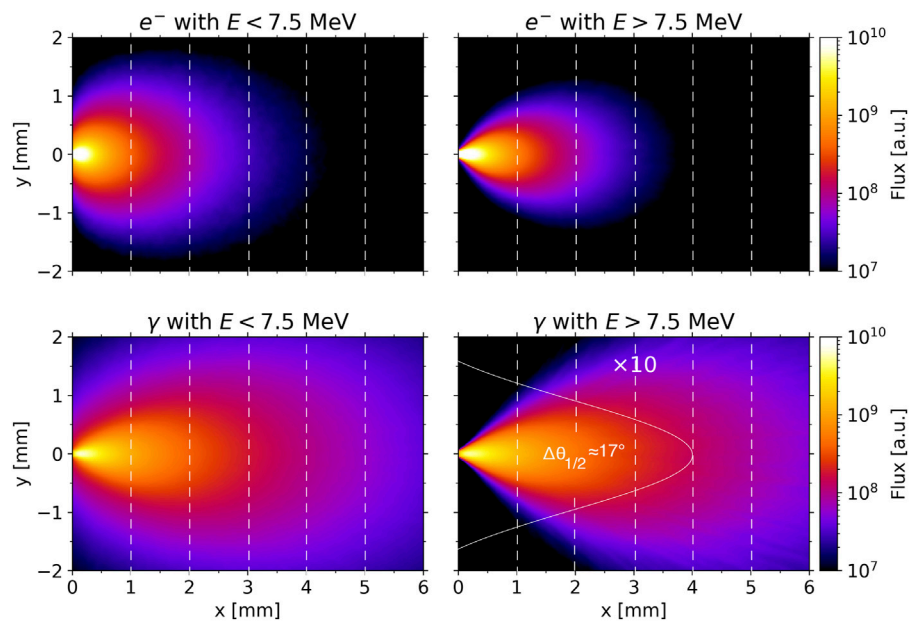
FIGURE 8
Fluences of electrons with energies below 7.5 MeV (top left) and above 7.5 MeV (top right); fluences of BS photons with energies below 7.5 MeV (bottom left) and above 7.5 MeV (bottom right). The values on the color scale have logarithmic spacing. The fluence for high-energy rays is multiplied by an additional factor of 10 for better illustration of their penetration depth with the chosen color scale.
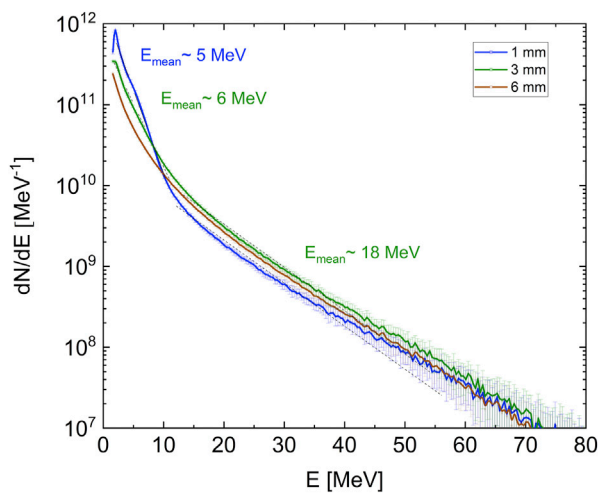

FIGURE 9
Energy spectrum of bremsstrahlung radiation obtained in Geant4 simulations. Different curves correspond to different tantalum thicknesses at $Z = 1$ mm, $Z = 3$ mm, and $Z = 6$ mm. The values on the ordinate axis have logarithmic spacing.

FIGURE 10
Yields of the most long-living isotopes produced inside the tantalum converter in the Geant4 simulations. Different colors correspond to the different layers of the target. The values on the ordinate axis have logarithmic spacing.

photons is produced as at this point, the electron beam becomes depleted due to its interaction with the converter material, and thus, the loss of photons is not compensated by the newly created photons. For high-energy part of the BS-spectrum, this effect appears to be less pronounced as a consequence of the longer mean-free path of energetic photons in the target. From the simulation, the number of BS photons and the conversion
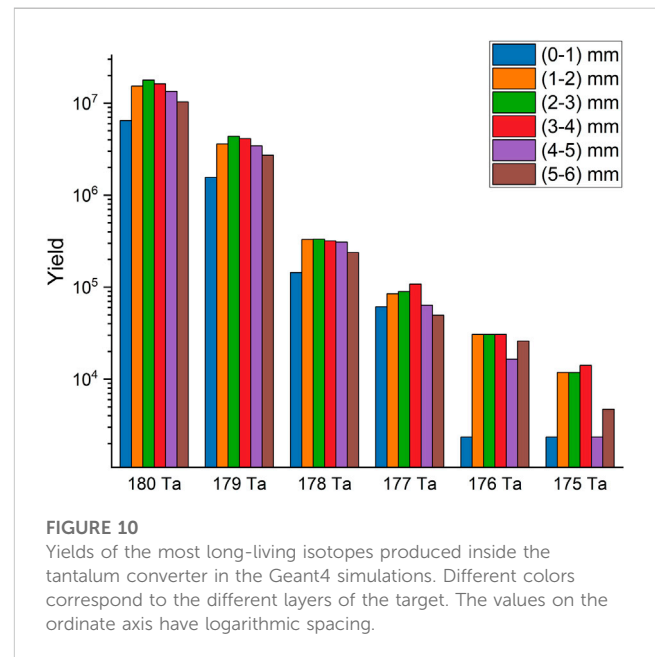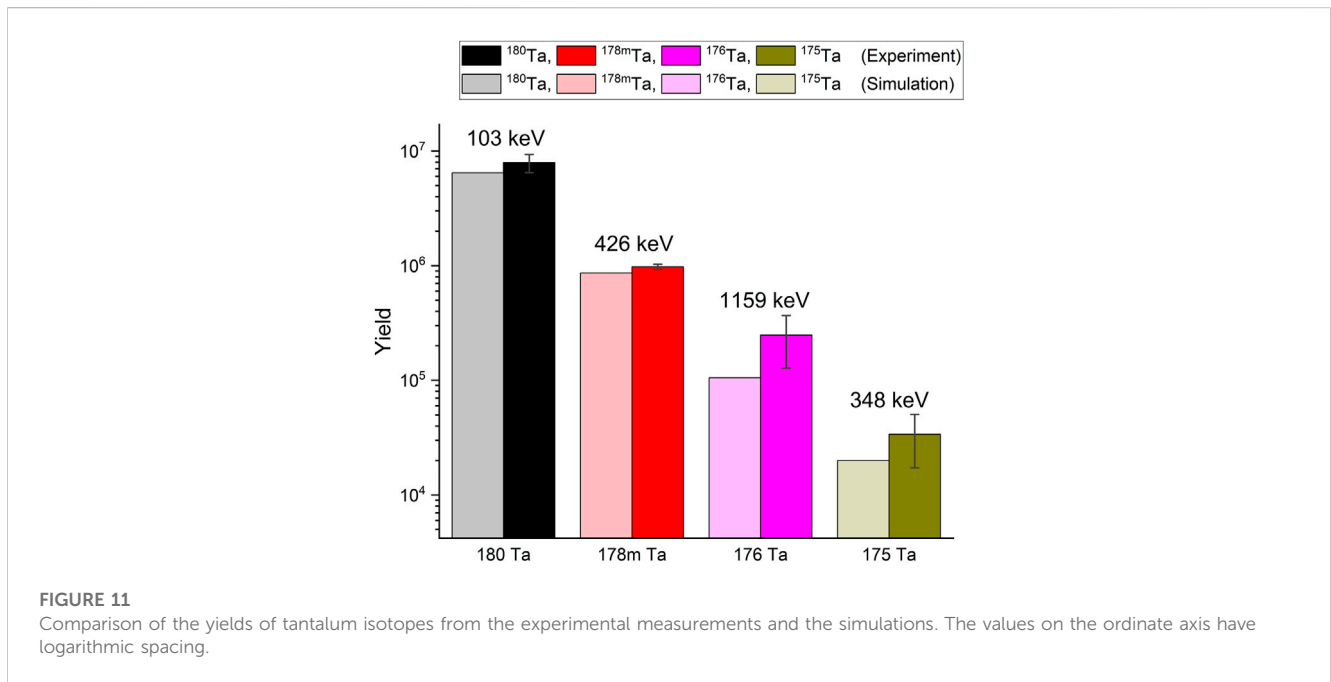
efficiency of the laser energy into the energy of BS-radiation was estimated for <7.5 MeV and >7.5 MeV energy regions. The values are summarized in Table 2. The highest number of photons in the energy range (1.5–7.5 MeV) suitable for pair production is generated within the 1-mm-thick converter with a laser energy to BS conversion efficiency of 5%. With increasing thickness, it drops to 1.5%. At the same time, the number of BS photons with energy >7.5 MeV remains fairly constant. The optimum is reached at the

TABLE 2 Number of the produced gamma photons N_γ and the conversion efficiency of laser energy into the energy of these photons η_γ in dependence on the penetration depth for two different energy ranges.

Penetration depth	1 mm		3 mm		6 mm	
Energy range	N_γ	η_γ	N_γ	η_γ	N_γ	η_γ
1.5–7.5 MeV	$1.6 \cdot 10^{12}$	5%	$9 \cdot 10^{11}$	3%	$5 \cdot 10^{11}$	1.5%
7.5–80 MeV	$1.3 \cdot 10^{11}$	1.5%	$1.7 \cdot 10^{11}$	2%	$1.3 \cdot 10^{11}$	1.7%

FIGURE 11
Comparison of the yields of tantalum isotopes from the experimental measurements and the simulations. The values on the ordinate axis have logarithmic spacing.

depth of the 3-mm-thick converter, where 1.7×10^{11} photons are produced with the highest conversion efficiency of 2%. The pulse duration of BS radiation for an optimized converter thickness of ~3 mm reaches ~10 ps. As follows from the simulations, bremsstrahlung emits in a cone subtended by a half-angle of 17°, which for the obtained number of photons, means that an ultra-high flux of ~6×10^{22} sr^{-1}·s^{-1} is obtained.

The bremsstrahlung photons with energy > 7.5 MeV induce photonuclear reactions inside the tantalum converter, creating various isotopes, including isotopes of tantalum with the mean life times of the order of a few hours that can be confidently measured. In the simulations, yields of different isotopes of tantalum resulting from (γ, xn) reactions were calculated using the cross sections provided in Geant4 [47]. The model target was divided into 1-mm thick layers to record Ta isotopes produced in each layer. The resulting yields of the most abundant and long-living isotopes created in each of the six layers are presented in Figure 10.

In order to compare these results with the experimental yields, it is important to take into account the absorption of γ ray characteristics for every isotope in the tantalum converter (see Figure 7). Since the energy of the characteristic gamma lines produced inside the tantalum sample as a result of radioactive decay of isotopes belongs to the (100–1,000) keV range (see Table 1), attenuation of these gamma rays can be significant,

especially for the gamma rays coming from the rear side of the converter. The most abundant and long-living isotopes of tantalum were distributed in the converter box according to the results of Geant4 modeling described previously. Several key gamma-decay lines with the known intensities and energies of the emitted gamma-quanta were selected from Table 1. The attenuation of the corresponding gamma rays was calculated as they pass from the location of a particular isotope to the front edge of the tantalum plate where the initial electron source was located and where the isotope yields were measured by means of a HPGe detector. The attenuation coefficients for gamma photons of a given energy were taken from the NIST database [49]. This procedure allowed for comparing the experimentally measured yields with those obtained in numerical modeling; see Figure 11. The results show that the yields of ^{180}Ta and ^{178m}Ta calculated from gamma spectroscopy measurements are in very good agreement with the simulations. The yields of ^{176}Ta and ^{175}Ta measured in the experiment are higher by factors ~2.3 and ~1.7 than predicted by simulations. The inconsistency of the measured and simulated ^{176}Ta and ^{175}Ta yields can be partially explained by the fact that the experimental cross-sectional data on the reactions ^{181}Ta$(\gamma,5n)^{176}$Ta and ^{181}Ta$(\gamma,6n)^{175}$Ta are higher than the cross sections used in simulations. Another reason could be the insufficient statistics in the simulation—for the computationally feasible number of initial electrons of 10^8, only tens of isotopes

of ^{176}Ta and ^{175}Ta were obtained. This may be inadequate for proper estimation of ^{176}Ta and ^{175}Ta yields in the experiment via appropriate normalization of these results for the real amount of laser-accelerated electrons.

4 Conclusion

A highly efficient approach, to generate an ultra-high flux, high-energy bremsstrahlung by applying long-scale, near-critical-density foam targets attached to a high-Z converter, was demonstrated in the experiments at the high-energy PHELIX laser supported with Geant4 Monte Carlo simulations. Photonuclear reactions have been observed in tantalum, leading to the production of ^{176}Ta and ^{175}Ta, which require photons with energies above 40 MeV. This can be compared to the isotope production in the experiment with similar PHELIX laser parameters, where a sub-ps laser pulse interacted with a dense gas jet to accelerate electrons before hitting a Ta converter [50]. Authors report the production of ^{178}Ta as a result of $(\gamma, 3n)$ reactions with a photon energy threshold of 22 MeV. The reason for the difference lies in the more efficient conversion of laser energy into high-current DLA electrons with energies up to 100 MeV, accelerated in the NCD plasma at PHELIX. The Geant4 Monte Carlo code, with the experimentally obtained electron energy and angular distributions as input parameters, was used to compare measured and simulated yields of ^{180}Ta to ^{175}Ta isotopes and to characterize the bremsstrahlung spectrum responsible for their production. Simulations made it possible to account for the inhomogeneous irradiation of the Ta converter with MeV electrons and photons and for the absorption of the characteristic gamma lines in the 6-mm-thick converter. In the end, a good agreement between measured and simulated Ta isotope yields was demonstrated. Based on this, we can conclude that when DLA electrons interacted with the thick high-Z converter, the directed bremsstrahlung was produced with an average photon energy of 18 MeV and $\sim 2 \times 10^{11}$ photons per laser shot in the energy range of giant dipole resonance (GDR) and beyond (≥ 7.5 MeV). This results in an ultra-high photon flux of $\sim 6 \times 10^{22}$ sr^{-1}·s^{-1} and 2% of the conversion efficiency of the focused laser energy into high-energy bremsstrahlung and shows a 10-fold increase in the MeV bremsstrahlung production compared to direct laser irradiation of the converter, demonstrated with the VULCAN and NOVA lasers [23, 24].

Data availability statement

The original contributions presented in the study are included in the article/Supplementary Material; further inquiries can be directed to the corresponding author.

Author contributions

PT, NB, and OR wrote the manuscript and conceived the scheme; PT, MMG, and US evaluated results of the nuclear diagnostics; MG was responsible for diagnostics of DLA electrons and conduction of the experiment together with JC, ŞZ, and OR. NA was responsible for simulations and discussion of DLA electrons; NGB was responsible for foam-target fabrication; NB and PK performed Geant4 simulations; and JJ and CS were responsible for revising the work critically.

Funding

Acknowledgments

Conflict of interest

Author SZ is employed by Focused Energy GmbH, Germany.

The remaining authors declare that the research was conducted in the absence of any commercial or financial relationships that could be construed as a potential conflict of interest.

Publisher's note

References

1. Negoita F, Roth M, Thirolf PG, Tudisco S, Hannachi F, Moustaizis S, et al. *Laser driven nuclear physics at ELI NP* (2022). *arXiv preprint arXiv:2201.01068.*

2. Pomerantz I, Mccary E, Meadows AR, Arefiev A, Bernstein AC, Chester C, et al. Ultrashort pulsed neutron source. *Phys Rev Lett* (2014) 113:184801. doi:10.1103/physrevlett.113.184801

3. Günther M, Rosmej O, Tavana P, Gyrdymov M, Skobliakov A, Kantsyrev A, et al. Forward-looking insights in laser-generated ultra-intense γ-ray and neutron sources for nuclear application and science. *Nat Commun* (2022) 13:170. doi:10.1038/s41467-021-27694-7

4. Sun Z, Okafor K, Isa S. Determining concentrations of elements with different reaction channels in photon activation. *Appl Radiat Isot* (2017) 127:173–8. doi:10.1016/j.apradiso.2017.06.012

5. Starovoitova VN, Segebade C. Photon activation analysis as a tool for evidentiary sample identification: A feasibility study. *J Radioanal Nucl Chem* (2017) 311:611–5. doi:10.1007/s10967-016-4964-5

6. Mirani F, Calzolari D, Formenti A, Passoni M. Superintense laser-driven photon activation analysis. *Commun Phys* (2021) 4:185. doi:10.1038/s42005-021-00685-2

7. Courtois C, Edwards R, Compant La Fontaine A, Aedy C, Barbotin M, Bazzoli S, et al. High-resolution multi-mev x-ray radiography using relativistic laser-solid interaction. *Phys Plasmas* (2011) 18:023101. doi:10.1063/1.3551738

8. Chen H, Nakai M, Sentoku Y, Arikawa Y, Azechi H, Fujioka S, et al. New insights into the laser produced electron–positron pairs. *New J Phys* (2013) 15:065010. doi:10.1088/1367-2630/15/6/065010

9. Ma Z, Lan H, Liu W, Wu S, Xu Y, Zhu Z, et al. Photonuclear production of medical isotopes 62, 64cu using intense laser-plasma electron source. *Matter Radiat Extremes* (2019) 4:064401. doi:10.1063/1.5100925

10. Pruet J, McNabb D, Hagmann C, Hartemann F, Barty C. Detecting clandestine material with nuclear resonance fluorescence. *J Appl Phys* (2006) 99:123102. doi:10.1063/1.2202005

11. Perry M, Sefcik J, Cowan T, Hatchett S, Hunt A, Moran M, et al. Hard x-ray production from high intensity laser solid interactions (invited). *Rev scientific Instr* (1999) 70:265–9. doi:10.1063/1.1149442

12. Brunel F. Not-so-resonant, resonant absorption. *Phys Rev Lett* (1987) 59:52–5. doi:10.1103/physrevlett.59.52

13. Wilks SC, Kruer WL. Absorption of ultrashort, ultra-intense laser light by solids and overdense plasmas. *IEEE J Quan Elect* (1997) 33:1954–68. doi:10.1109/3.641310

14. Malka G, Miquel J. Experimental confirmation of ponderomotive-force electrons produced by an ultrarelativistic laser pulse on a solid target. *Phys Rev Lett* (1996) 77:75–8. doi:10.1103/physrevlett.77.75

15. Wilks S, Kruer W, Tabak M, Langdon A. Absorption of ultra-intense laser pulses. *Phys Rev Lett* (1992) 69:1383–6. doi:10.1103/physrevlett.69.1383

16. Tajima T, Dawson JM. Laser electron accelerator. *Phys Rev Lett* (1979) 43:267–70. doi:10.1103/physrevlett.43.267

17. Amiranoff F, Baton S, Bernard D, Cros B, Descamps D, Dorchies F, et al. Observation of laser wakefield acceleration of electrons. *Phys Rev Lett* (1998) 81:995–8. doi:10.1103/physrevlett.81.995

18. Pukhov A, Sheng ZM, Meyer-ter Vehn J. Particle acceleration in relativistic laser channels. *Phys Plasmas* (1999) 6:2847–54. doi:10.1063/1.873242

19. Willingale L, Arefiev A, Williams G, Chen H, Dollar F, Hazi A, et al. The unexpected role of evolving longitudinal electric fields in generating energetic electrons in relativistically transparent plasmas. *New J Phys* (2018) 20:093024. doi:10.1088/1367-2630/aae034

20. Rosmej O, Andreev N, Zaehter S, Zahn N, Christ P, Borm B, et al. Interaction of relativistically intense laser pulses with long-scale near critical plasmas for optimization of laser based sources of mev electrons and gamma-rays. *New J Phys* (2019) 21:043044. doi:10.1088/1367-2630/ab1047

21. Rosmej O, Gyrdymov M, Günther M, Andreev N, Tavana P, Neumayer P, et al. High-current laser-driven beams of relativistic electrons for high energy density research. *Plasma Phys Controlled Fusion* (2020) 62:115024. doi:10.1088/1361-6587/abb24e

22. Bochkarev S, Brantov A, Bychenkov V, Torshin D, Kovalev V, Baidin G, et al. Stochastic electron acceleration in plasma waves driven by a high-power subpicosecond laser pulse. *Plasma Phys Rep* (2014) 40:202–14. doi:10.1134/s1063780x14030027

23. Norreys PA, Santala M, Clark E, Zepf M, Watts I, Beg F, et al. Observation of a highly directional γ-ray beam from ultrashort, ultraintense laser pulse interactions with solids. *Phys Plasmas* (1999) 6:2150–6. doi:10.1063/1.873466

24. Stoyer M, Sangster T, Henry E, Cable M, Cowan T, Hatchett S, et al. Nuclear diagnostics for petawatt experiments (invited). *Rev Scientific Instr* (2001) 72:767–72. doi:10.1063/1.1319355

25. Günther M, Sonnabend K, Brambrink E, Vogt K, Bagnoud V, Harres K, et al. A novel nuclear pyrometry for the characterization of high-energy bremsstrahlung and electrons produced in relativistic laser-plasma interactions. *Phys Plasmas* (2011) 18:083102. doi:10.1063/1.3613923

26. Ledingham K, Spencer I, McCanny T, Singhal R, Santala M, Clark E, et al. Photonuclear physics when a multiterawatt laser pulse interacts with solid targets. *Phys Rev Lett* (2000) 84:899–902. doi:10.1103/physrevlett.84.899

27. Spencer I, Ledingham K, Singhal R, McCanny T, McKenna P, Clark E, et al. A nearly real-time high temperature laser–plasma diagnostic using photonuclear reactions in tantalum. *Rev Scientific Instr* (2002) 73:3801–5. doi:10.1063/1.1511802

28. Günther M, Britz A, Clarke R, Harres K, Hoffmeister G, Nürnberg F, et al. Nais: Nuclear activation-based imaging spectroscopy. *Rev scientific Instr* (2013) 84:073305. doi:10.1063/1.4815826

29. Henderson A, Liang E, Riley N, Yepes P, Dyer G, Serratto K, et al. Ultra-intense gamma-rays created using the Texas petawatt laser. *High Energ Density Phys* (2014) 12:46–56. doi:10.1016/j.hedp.2014.06.004

30. Hannasch A, Laso Garcia A, LaBerge M, Zgadzaj R, Köhler A, Couperus Cabadağ J, et al. Compact spectroscopy of kev to mev x-rays from a laser wakefield accelerator. *Scientific Rep* (2021) 11:14368. doi:10.1038/s41598-021-93689-5

31. Andreev N, Gorbunov L, Kirsanov V, Pogosova A, Ramazashvili R. Resonant excitation of wakefields by a laser pulse in a plasma. *JETP Lett* (1992) 55:571–6.

32. King P, Lemos N, Shaw J, Milder A, Marsh K, Pak A, et al. X-ray analysis methods for sources from self-modulated laser wakefield acceleration driven by picosecond lasers. *Rev Scientific Instr* (2019) 90:033503. doi:10.1063/1.5082965

33. Li S, Shen B, Xu J, Xu T, Yu Y, Li J, et al. Ultrafast multi-mev gamma-ray beam produced by laser-accelerated electrons. *Phys Plasmas* (2017) 24:093104. doi:10.1063/1.4996020

34. Pukhov A. Strong field interaction of laser radiation. *Rep Prog Phys* (2002) 66:47–101. doi:10.1088/0034-4885/66/1/202

35. Li Y, Gu Y, Zhu Z, Li X, Ban H, Kong Q, et al. Direct laser acceleration of electron by an ultra intense and short-pulsed laser in under-dense plasma. *Phys Plasmas* (2011) 18:053104. doi:10.1063/1.3581062

36. Arefiev A, Khudik V, Robinson A, Shvets G, Willingale L, Schollmeier M. Beyond the ponderomotive limit: Direct laser acceleration of relativistic electrons in sub-critical plasmas. *Phys Plasmas* (2016) 23:056704. doi:10.1063/1.4946024

37. Pugachev L, Andreev N, Levashov P, Rosmej O. Acceleration of electrons under the action of petawatt-class laser pulses onto foam targets. *Nucl Instr Methods Phys Res Section A: Acc Spectrometers, Detectors Associated Equipment* (2016) 829:88–93. doi:10.1016/j.nima.2016.02.053

38. Pugachev L, Andreev N. Characterization of accelerated electrons generated in foams under the action of petawatt lasers. *J Phys Conf Ser* (2019) 1147:012080. doi:10.1088/1742-6596/1147/1/012080

39. Passoni M, Zani A, Sgattoni A, Dellasega D, Macchi A, Prencipe I, et al. Energetic ions at moderate laser intensities using foam-based multi-layered targets. *Plasma Phys Controlled Fusion* (2014) 56:045001. doi:10.1088/0741-3335/56/4/045001

40. Prencipe I, Sgattoni A, Dellasega D, Fedeli L, Cialfi L, Choi IW, et al. Development of foam-based layered targets for laser-driven ion beam production. *Plasma Phys Controlled Fusion* (2016) 58:034019. doi:10.1088/0741-3335/58/3/034019

41. Bin J, Yeung M, Gong Z, Wang H, Kreuzer C, Zhou M, et al. Enhanced laser-driven ion acceleration by superponderomotive electrons generated from near-critical-density plasma. *Phys Rev Lett* (2018) 120:074801. doi:10.1103/physrevlett.120.074801

42. Bagnoud V, Aurand B, Blazevic A, Borneis S, Bruske C, Ecker B, et al. Commissioning and early experiments of the phelix facility. *Appl Phys B* (2010) 100:137–50. doi:10.1007/s00340-009-3855-7

43. Borisenko N, Khalenkov A, Kmetik V, Limpouch J, Merkuliev YA, Pimenov V. Plastic aerogel targets and optical transparency of undercritical microheterogeneous plasma. *Fusion Sci Technol* (2007) 51:655–64. doi:10.13182/fst07-a1460

44. Krmar M, Slivka J, Bikit I, Veskovic M, Conkic L, Bistrovic M, et al. A new method for the measurement of bremsstrahlung spectra. *Phys Med Biol* (1993) 38:533–44. doi:10.1088/0031-9155/38/4/005

45. Koning A, Rochman D, Sublet JC, Dzysiuk N, Fleming M, van der Marck S. Tendl: Complete nuclear data library for innovative nuclear science and technology. *Nucl Data Sheets* 155:(2019) 1–55. doi:10.1016/j.nds.2019.01.002

46. Otuka N, Dupont E, Semkova V, Pritychenko B, Blokhin A, Aikawa M, et al. Towards a more complete and accurate experimental nuclear reaction data library (exfor): International collaboration between nuclear reaction data centres (nrdc). *Nucl Data Sheets* (2014) 120:272–6. doi:10.1016/j.nds.2014.07.065

47. Agostinelli S, Allison J, Amako K, Apostolakis J, Araujo H, Arce P, et al. Geant4—A simulation toolkit. *Nucl Instr Methods Phys Res Section A: Acc Spectrometers, Detectors Associated Equipment* (2003) 506:250–303. doi:10.1016/S0168-9002(03)01368-8

48. Allison J, Amako K, Apostolakis J, Arce P, Asai M, Aso T, et al. Recent developments in geant4. *Nucl Instr Methods Phys Res Section A: Acc Spectrometers, Detectors Associated Equipment* (2016) 835:186–225. doi:10.1016/j.nima.2016.06.125

49. Hubbell J, Seltzer S. *Tables of x-ray mass attenuation coefficients and mass energy-absorption coefficients 1 kev to 20 mev for elements z = 1 to 92 and 48 additional substances of dosimetric interest* (1995). Available at: http://physics.nist.gov/PhysRefData/XrayMassCoef/cover.html.

50. Santala MIK, Najmudin Z, Clark EL, Tatarakis M, Krushelnick K, Dangor AE, et al. Observation of a hot high-current electron beam from a self-modulated laser wakefield accelerator. *Phys Rev Lett* (2001) 86:1227–30. doi:10.1103/PhysRevLett.86.1227